Nano Research
2023, 16(2): 2119–2125

ISSN 1998-0124 CN 11-5974/O4
https://doi.org/10.1007/s12274-022-4935-9

Research Article

Oxidation-induced phase separation of carbon-supported CuAu nanoparticles for electrochemical reduction of CO_2

Yayun Guan[1,§], Yatian Liu[1,§], Qingye Ren[1], Zejian Dong[1] (✉), and Langli Luo[1,2] (✉)

[1] *Institute of Molecular Plus, Department of Chemistry, Tianjin University, Tianjin 300072, China*
[2] *Haihe Laboratory of Sustainable Chemical Transformations, Tianjin 300192, China*
[§] *Yayun Guan and Yatian Liu contributed equally to this work.*

Received: 14 June 2022 / **Revised:** 29 July 2022 / **Accepted:** 18 August 2022

ABSTRACT

Alloy nanostructures have been extensively exploited in both thermal and electrochemical catalysis due to their beneficial "synergetic effects" and being cost-effective. Understandings of the alloy nanostructures including phases, interfaces, and chemical composition are prerequisites for utilizing them as efficient electrocatalysts. Here, we use carbon-supported CuAu nanoparticles as a model catalyst to demonstrate the phase-separation induced variation of electrochemical performance for the CO_2 reduction reaction. Driven by thermal oxidation, the CuO_x phase gradually separates from the original CuAu nanoparticles, and different carbon supports, i.e., graphene vs. carbon nanotube lead to a reversed trend in the selectivity towards CO production. Through detailed structural and chemical analysis, we find the extent of phase separation holds the key to this variation and could be used as an effective method to tune the electrochemical properties of the alloy phase.

KEYWORDS

CuAu, CO_2 reduction reaction, electrochemical, phase separation, atomic scale

1 Introduction

Alloy nanostructures have been employed as heterogeneous catalysts for both thermal [1–4] and electrochemical [5, 6] processes due to their tunable composition and electronic structures that are vital to catalytic processes. For the electrochemical reduction of CO_2, alloy nanoparticle catalysts have been exploited to enhance the activity, selectivity, and stability of the electrocatalysts [7–13]. The merit of alloy nanoparticles compared to their single-component counterparts lies in the so-called synergetic effect [14], i.e., the combination of two metal elements largely promotes the catalytic properties of specific products [15–20]. For instance, introducing Zn atoms into Cu could favour the selectivity of ethanol versus ethylene production by a factor of ~ 12.5 [21].

Alloying as an ancient metallurgy technique often brings new physical and chemical properties by tuning the phase and microstructure of the base metals. The alloying effect can be exaggerated when the dimension of interest enters the nanoscale. The structure, phase, and interface as well as the chemical distribution are critical factors of the alloy nanoparticles that determine their intrinsic catalytic properties, which are sensitive to the processing method and working conditions. For instance, the CuAu nanoparticles with a disordered phase favour hydrogen production while its ordered phase leads to a CO production with a Faradaic efficiency of ~ 80% [22]. Phase segregation with concurrent composition change and surface oxidation [23, 24] of alloy could play a vital role in determining the electrocatalytic performance [25]. On the other hand, alloy nanoparticle electrocatalysts are subject to significant structural and chemical changes under electrochemical conditions, further complicating the analysis of their structure-property relationship [26–28]. Ambiguity still exists in the varied evolved alloy nanostructures and the correlation to their electrochemical catalytic performance. Alloys of two elements with different tendency for oxidation, e.g., CuAu could lead to an evolving and complicated spatial and temporal distribution of Cu-Au-O systems, which is critical to understand their contribution to the overall electrochemical process.

Herein, we use CuAu nanoparticles with the solid solution phase anchored on two different supports, carbon nanotubes (CNTs) vs. three-dimensional (3D) graphene (Gr) as a model alloy catalyst system to track the structural and chemical change upon the post-treatment and during reaction condition of CO_2 electrochemical reduction. Different statuses of phase separation have been detected for CuAu nanoparticles for two different supports upon post-annealing and reaction. This difference caused by carbon supports leads to the variation in product selectivity towards CO.

2 Results and discussion

We prepared CuAu nanoparticles (NPs) with a solid-solution phase (Cu and Au atoms are randomly mixed) and with an average size of less than 10 nm according to a previously reported procedure with some modifications [29]. In the presence of Au NPs, $Cu(acac)_2$ was reduced by oleylamine to Cu that diffused into the Au seeds to form CuAu NPs at 210 °C. As shown in Scheme 1,

Address correspondence to Zejian Dong, dongzj@tju.edu.cn; Langli Luo, luolangli@tju.edu.cn

as-synthesized CuAu nanoparticles are loaded on 3D-Gr (noted as CuAu/Gr) and CNTs (noted as CuAu/CNTs) through the impregnation method, followed by annealing in the air. How would the CuAu nanoparticles evolve chemically and structurally upon post-annealing and during the electrochemical reaction and how these changes affect the CO_2 conversion products are the central questions to be tackled in our scheme.

2.1 CuAu nanoparticles supported on 3D-Gr vs. CNTs

Figure 1 shows the morphology of as-prepared and annealed CuAu/Gr and CuAu/CNTs electrocatalysts by high-angle annular dark-field scanning transmission electron microscopy (HAADF-STEM) images and corresponding particle size analysis. As shown in Figs. 1(a) and 1(e), the CuAu nanoparticles are uniformly distributed with a large density after being loaded on the graphene, and the average particle size is 6.8 ± 0.8 nm as shown in the corresponding size distribution analysis of Fig. 1(i). Figures 1(b), 1(f), and 1(j) show the average size of CuAu nanoparticles increases to 11.1 ± 2.3 nm after annealing accompanying a decrease in particle density. This indicates a classic Oswald ripening process happens for CuAu nanoparticles on graphene during annealing. The CuAu nanoparticles loaded on CNTs have a similar trend before (Figs. 1(c) and 1(g)) and after annealing (Figs. 1(d) and 1(h)), but the size increase of CuAu nanoparticles before and after annealing (from 6.8 ± 1.0 to 8.0 ± 2.0 nm) is much less than that of CuAu/Gr, as shown in Figs. 1(k) and 1(l). These results show the effect of carbon supports on the average size and size distribution of CuAu nanoparticles upon the post-annealing process.

Then, we further investigate the structural and chemical change of CuAu nanoparticles upon the annealing process. Figure 2(a) shows the X-ray diffraction (XRD) analysis of CuAu/Gr before and after annealing. The original CuAu solid solution phase as indicated by the red spectrum with broad peaks changes to the "Au-like" phase (we will see it's not a pure Au phase) indicated by the blue spectrum with sharper peaks. A peak shift to the smaller angles (larger lattice distance) when transitioning from CuAu to Au-like phases with both face-center cubic (FCC) structures. The

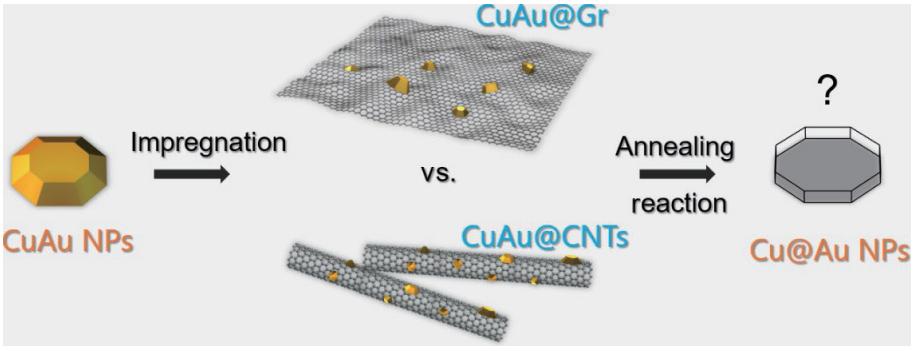

Scheme 1 Structural and chemical investigation of CuAu nanoparticles loaded on graphene vs. carbon nanotubes after post-annealing and reaction.

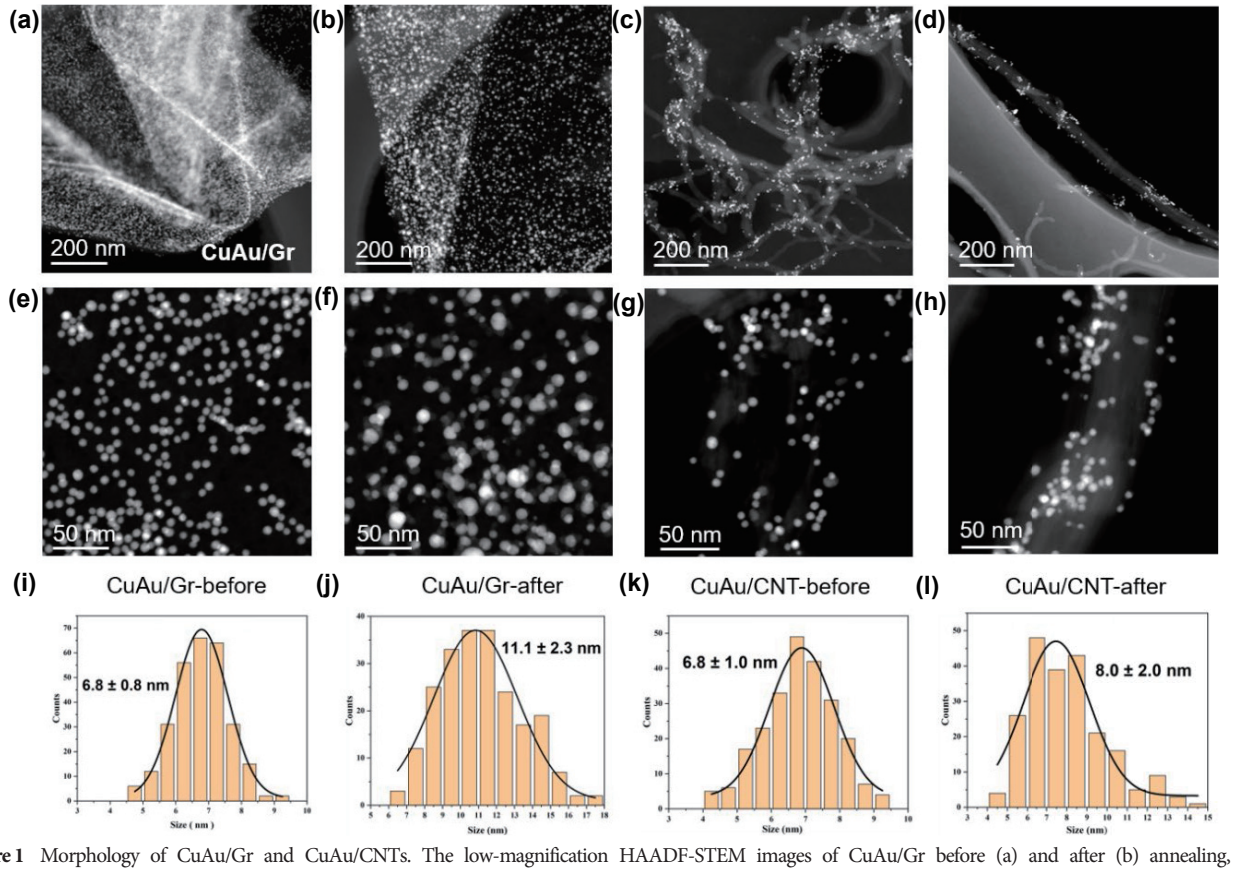

Figure 1 Morphology of CuAu/Gr and CuAu/CNTs. The low-magnification HAADF-STEM images of CuAu/Gr before (a) and after (b) annealing, and CuAu/CNTs before (c) and after (d) annealing. The high-magnification HAADF-STEM images of CuAu/Gr before (e) and after (f) annealing, and CuAu/CNTs before (g) and after (h) annealing. The particle size analysis of CuAu/Gr before (i) and after (j) annealing, and CuAu/CNTs before (k) and after (l) annealing.

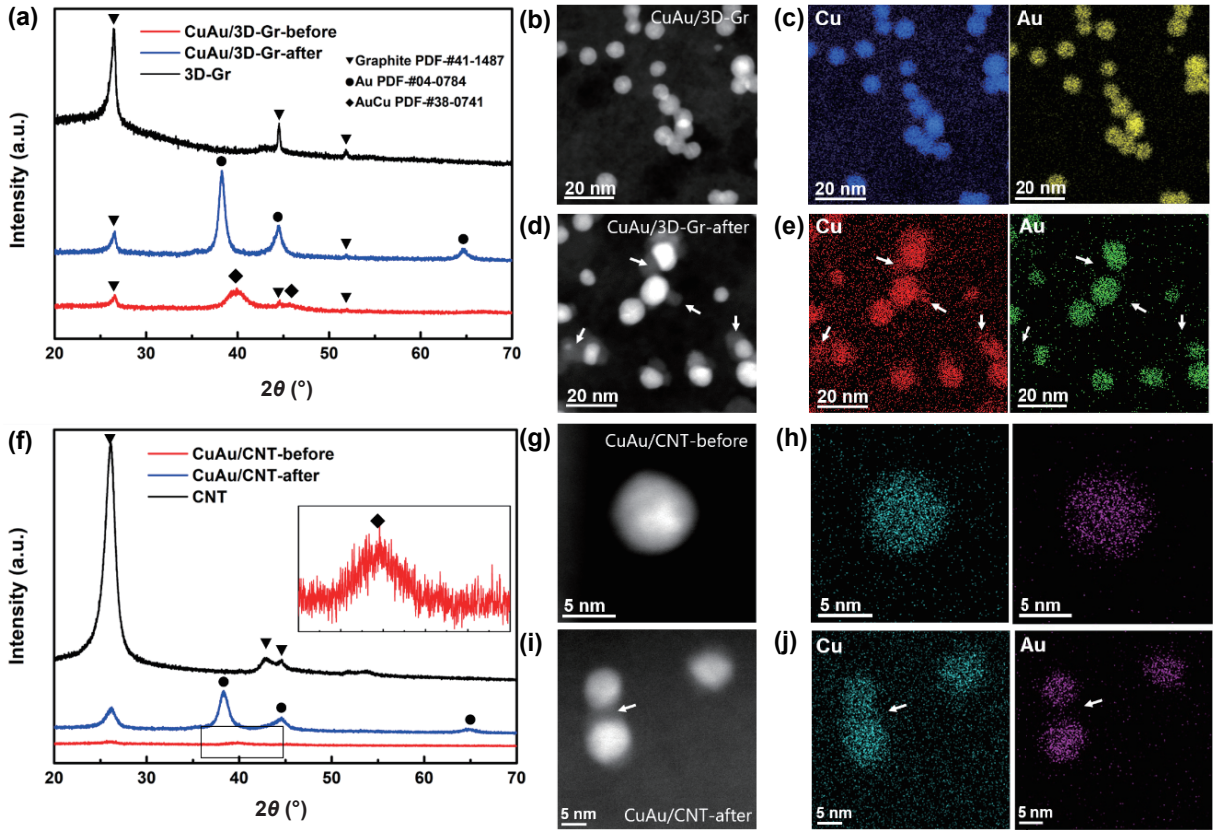

Figure 2 Phase separation of CuAu/Gr and CuAu/CNTs. (a) XRD patterns of CuAu-Gr before and after annealing as referenced by the graphite. (b) and (d) HAADF-STEM images of CuAu/Gr before and after annealing. (c) and (e) The corresponding EDS mapping of Cu and Au in CuAu/Gr before and after annealing. (f) XRD patterns of CuAu/CNTs before and after annealing as referenced by CNTs. (g) and (i) HAADF-STEM images of CuAu/Gr before and after annealing. (h) and (j) The corresponding EDS mapping of Cu and Au in CuAu/Gr before and after annealing.

reference peaks of graphene indicated by the black spectrum are found in both samples. By HAADF-STEM images and corresponding energy-dispersive spectra (EDS) mapping, we can see the Cu and Au elements are uniformly mixed in the CuAu/Gr before annealing, as shown in Figs. 2(b) and 2(c), which confirms its solid solution phase. After annealing, we can see the partitioning of CuAu nanoparticles as shown in Fig. 2(d), where the brighter contrast indicates the presence of an Au-rich zone and the dark contrast (white arrows) around the Au-rich zone are rich in Cu. This is because the HAADF-STEM image directly reflects its atomic weight to the intensity of contrast, i.e., Au with a higher atomic number has a brighter contrast than Cu. Hence, this manifests a phase separation of CuAu nanoparticles, which is further illustrated by the EDS mapping in Fig. 2(e). It is noted that the brighter contrasted areas also have a significant amount of Cu elements, which indicates this phase separation of CuAu is not complete, leaving CuAu nanoparticles (enriched by Au) and the Cu-rich zone around them. For the CuAu/CNTs, post-annealing also leads to a size increase of CuAu nanoparticles as indicated by the sharpening of XRD peaks in Fig. 2(f). Microscopically, the extent of phase separation of CuAu is much less than that of CuAu/Gr as shown in Fig. S1 in the Electronic Supplementary Material (ESM). As shown in the STEM images of Figs. 2(g) and 2(i), no contrast difference is detected for a single CuAu nanoparticle (Fig. 2(g)) before annealing, while a dark region appears after the annealing as indicated by the arrow in Fig. 2(i). The EDS mapping of Figs. 2(h) and 2(j) also clearly shows the phase-separation happens in the interfacial region of two nanoparticles as indicated by the arrow in Fig. 2(j). From the above observations, we have identified a thermally driven phase separation of CuAu nanoparticles mediated by two carbon supports, which will be tested for their electrochemical performance as below.

2.2 Electrocatalytic performance for CO_2 reduction reaction (CO_2RR)

We evaluate the performance of CuAu/Gr and CuAu/CNTs catalysts for the electrochemical reduction of CO_2 under an H-cell configuration using 0.1 M $KHCO_3$ solution as the electrolyte. Firstly, we compare pure CuAu nanoparticles, CuAu/CNTs, and CuAu/Gr before and after annealing, at a potential of −0.8 V vs. reversible hydrogen electrode (RHE) as shown in Fig. 3(a). Compared with pure CuAu nanoparticles, CuAu/CNTs shows similar Faradaic efficiency (FE) for both CO and H_2 production (54.03% vs. 46.5% for CO, and 43.5% vs. 40.32% for H_2), while the CuAu/Gr shows an increase of CO FE from 54.03% to 71.35%. After annealing, the CuAu/CNTs shows a strong boost of CO FE from 46.5% to 80.36%, while the CuAu/Gr shows a sharp decrease of CO FE from 71.35% to 47.78%. This manifests a reversed effect of the annealing process on the electrochemical performance of CuAu nanoparticles on different carbon supports. We can see a similar trend in the linear sweep voltammetry (LSV) test (scan rate = 10 $mV \cdot s^{-1}$) as shown in Fig. 3(b). For instance, CuAu/CNTs-after has the lowest onset potential of ~ 390 mV and largest current density followed by CuAu/Gr-before, while the CuAu/CNT-before and CuAu/Gr-after are the two worse ones. Then, we check the CO FE of CuAu/CNTs and CuAu/Gr samples at different potentials (−0.7 to −1.1 V) as shown in Figs. 3(c) and 3(d). The CO FE of CuAu/CNTs after annealing peaks at −0.8 V to reach 80%, which is also the highest for CuAu nanoparticles on CNTs as shown in Fig. 3(c). However, the highest CO FE of ~ 86% for CuAu/Gr is achieved without annealing as shown in Fig 3(d). These results show that the annealing process leads to a distinct effect on the electrochemical performance of CuAu nanoparticles on different carbon supports, e.g., CNTs vs. Gr, which may be related to phase-separation phenomenon observed

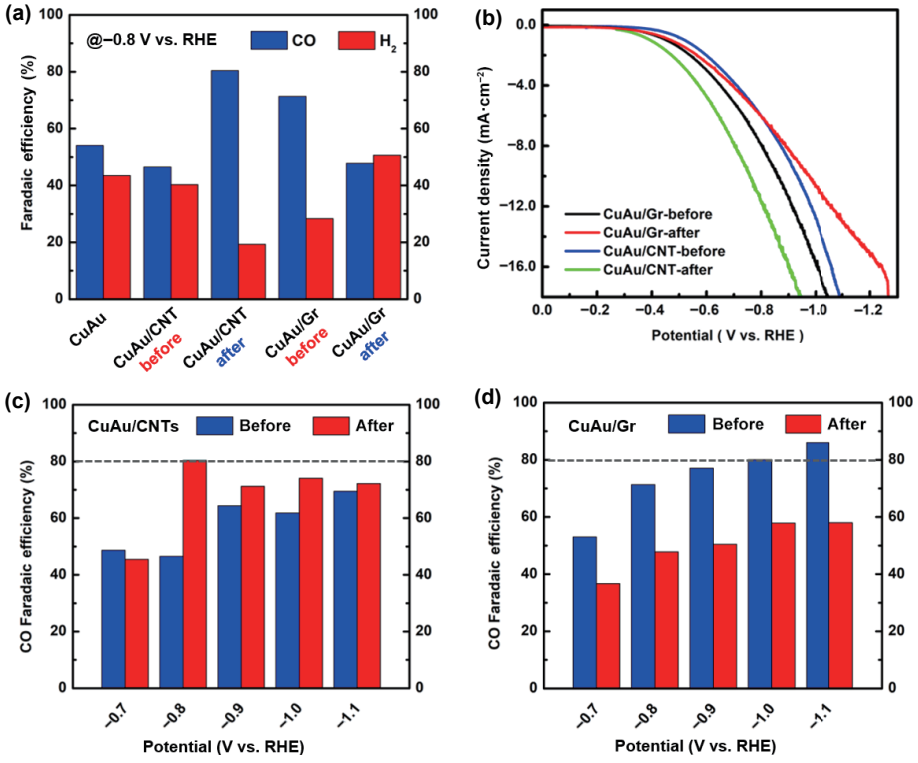

Figure 3 Electrocatalytic performance of CuAu/Gr vs. CuAu/CNTs for CO_2RR. (a) Electrochemical CO_2 reduction activities of CuAu nanoparticles, CuAu/CNTs, and CuAu/Gr evaluated by FE of CO and H_2. Measurements were conducted at −0.8 V vs. RHE with 0.1 M $KHCO_3$ solution (pH 6.8). (b) LSV curves for CuAu/CNTs and CuAu/Gr in CO_2-saturated $KHCO_3$. (c) Comparison of CO FE on CuAu/CNTs at various applied potentials. (d) Comparison of CO FE on CuAu/Gr at various applied potentials.

in Fig. 2. However, understanding the structural and chemical changes induced by phase-separation of CuAu needs further atomic-scale information on the working electro-catalysts.

Long-term stability test was conducted at the potential of −0.8 V vs. RHE on four samples (Fig. S6 in the ESM). There is no significant decay in current density during 6 h. But the CO FE of four samples decreases in varying degrees. The structure evolution of catalysts after electrochemical test was characterized by transmission electron microscope (TEM). Figure S7 in the ESM shows the HAADF images of the morphology of CuAu/Gr and CuAu/CNTs catalysts after CO_2RR for 6 h. The CuAu supporting on Gr after annealing changes most significantly after six hours of reaction, agglomerating into large particles of different sizes. This observation may be responsible for the poor CO FE, which needs further exploration. And the remaining three catalysts are slightly agglomerated with most particles maintaining their original size.

2.3 Surface and interface of CuAu/C catalysts

We use high-resolution TEM (HRTEM) imaging to investigate the atomic structure of CuAu nanoparticles as shown in Fig. 4. The pristine CuAu nanoparticles possess a typical faceted polyhedron morphology, which shows a "round" shape from a specific projection view as shown in Figs. 4(a) and 4(b). This is the thermodynamically preferred morphology of nanoparticles with the smallest surface energy adopted by a solid-solution phase. Figure 4(c) shows the corresponding fast Fourier transformation (FFT) pattern in Fig. 4(b), which shows a multi-twined diffraction pattern with CuAu (220) and (200) indexed. Besides, we can measure the lattice distance and estimate the composition of Cu or Au through the empirical Vegard's Law, which has been detailed in the Methods, and Figs. S2 and S3 in the ESM. It is noted that most of the CuAu nanoparticles before annealing have a typical five-fold twinning structure. However, the atomic structure of CuAu nanoparticles after the annealing changes significantly, leading to the phase separation as we observed above. Figure 4(d) shows the HRTEM image of typical CuAu nanoparticles on CNTs after annealing. Figure 4(d) shows an AuCu nanoparticle (circled by the yellow dashed line) with a clear five-fold twin structure surrounded by another crystalline phase possibly Cu_2O as measured by a plane distance of ~ 2.45 Å corresponding to the lattice distance of Cu_2O (111). This is a "core–shell" like structure but there is no oxide between the intimate interface between CNT and Au. Figure 4(e) shows the same trend of the phase-separation happening for a single CuAu nanoparticle, but the spatial distribution of Au and oxide phase is different from that in Fig. 4(d). Two Au grains are placed side-by-side with intimate contact with both the CNT surface and Cu_2O phase. We can label the Au and Cu_2O phases by the corresponding FFT pattern (Fig. 4(f)).

Distinct from this type of partial phase-separation, i.e., two separated phases still reside in the same nanoparticle, the phase-separation is rather complete for CuAu nanoparticles on graphene. As shown in Fig. 4(g), the typical morphology of nanoparticles on graphene is separated large or small nanoparticles with faceted surfaces as well as a typical twinning structure. Detailed structural analysis by the combination of HRTEM and FFT reveals that most of the larger nanoparticles are of the Au phase as shown in Fig. S4 in the ESM. Comparatively, the Cu phase is rather complicated in terms of its spatial distribution and the exact phase. As shown in Fig. 4(h) (an enlarged region of Fig. 4(g)), adjacent to two small Au nanoparticles (yellow dashed lines), we find several regions with clear lattice fringes but with which phases could not be easily identified. Similarly, these regions also exist sparsely on the graphene but are clearly separated from the segregated Au nanoparticles as indicated by white dashed lines in Fig. 4(i).

Then, we use X-ray photoelectron spectroscopy (XPS) to check the chemical status of Cu on the surface of the CuAu/C catalyst. As shown in Figs. 5(a) and 5(b), for both CuAu/Gr and CuAu/CNTs samples, the annealing leads to the surface oxidation of Cu^0 and Cu^I to Cu^{II} as evidenced by peak shifting towards

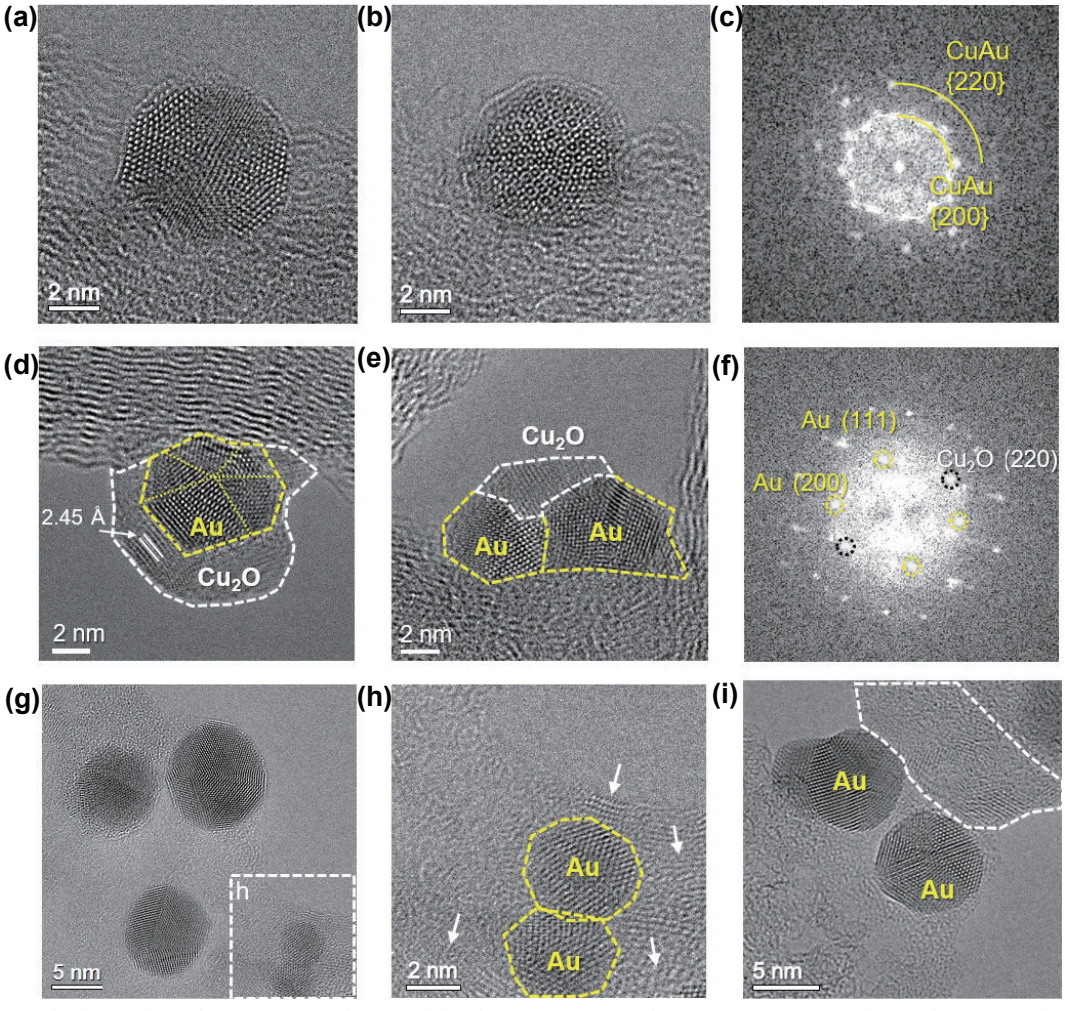

Figure 4 Atomic-scale phase analysis of CuAu nanoparticles. (a) and (b) The HRTEM images of pristine CuAu nanoparticles. (c) The corresponding FFT pattern in (b). (d) and (e) HRTEM images of typical CuAu nanoparticles on CNTs after annealing. (f) The corresponding FFT pattern in (e). (g)–(i) HRTEM images of typical CuAu nanoparticles on graphene after annealing.

higher binding energy as well as the appearance of the satellite peaks as indicated by the arrows. The Cu LMM Auger electron spectroscopy (AES) analysis also shows the mixed-valence status of Cu in the annealed samples as shown in Fig. S5 in the ESM. These chemical analyses reveal that the Cu oxide on either Au surface or carbon supports is of mixed Cu^0 and Cu^I species with a non-stoichiometric atomic structure as noted as CuO_x. This is further illustrated in the HRTEM image of Fig. 5(c), where the surface CuO_x is segmented with a lattice distance of ~ 2.45 Å corresponding to the plane distance of Cu_2O (111) in some regions. This highly defected CuO_x overlayer has a "Cu_2O-like" phase with only the first diffraction ring appearing in the corresponding FFT pattern (Fig. 5(d)). The other region (the dashed box on the right side of Fig. 5(c)) shows a semi-coherent interface between Au and Cu_2O phase, as evidenced by the FFT pattern in Fig. 5(e). All the above observations, chemically and structurally, manifest the separation of the Cu phase is not intuitively as the classic dealloying process, where a one-to-two phase transition proceeds by forming a sharp interface. We suggest an atom-by-atom process of Cu segregation from the CuAu alloy nanoparticles driven by thermal oxidation. As illustrated in Fig. 5(f), the phase separation takes place in general and different types of carbon support lead to varied final products. The CuAu NPs on CNTs form an intimate Au/Cu_2O interface, which resembles a "Schottky junction" between metal and oxide, leading to a boost of CO production. On the other side, the CuAu NPs on graphene completely segregated to discrete Cu and Au NPs (following the oxidation of Cu to CuO_x), where Au and CuO_x separately contribute to the CO_2 conversion, leading to a decrease of CO FE. Although the mechanisms Au/Cu_2O interface have been mentioned by previous work [29], further comprehensive understanding through detailed theoretical work is necessary.

The dependence of phase-separation behavior of CuAu on different carbon supports could stem from the interaction between C and CuAu NPs that evolves during the heat-treatment. Experimentally, the CuAu NPs on Gr are more mobile than those supported on CNTs, indicating they have a strong interaction with the CNT surface. During the thermal treatment in the air, the Au atoms in CuAu NPs on Gr can diffuse easily to form separated Au NPs, while the Cu is oxidized adjacently. Since the oxidation reaction is the driving force for the phase separation, the degree of oxidation, how many Cu atoms can be extracted from the original CuAu NPs holds the key for the phase-separation process. Obviously, the strong interaction between CuAu and CNT inhibits such an oxidation-induced phase-separation.

3 Conclusions

In summary, we use CuAu nanoparticles supported on graphene and CNT as the model electrocatalysts to evaluate the effect of phase-separation of CuAu on their catalytic performance for CO_2RR. We find that the Cu atoms are segregated from CuAu nanoparticles to form CuO_x driven by surface oxidation of Cu under thermal annealing conditions. This process leads to reversed trend in the selectivity change toward CO for CuAu/CNT and CuAu/Gr, respectively. Through the detailed structural and

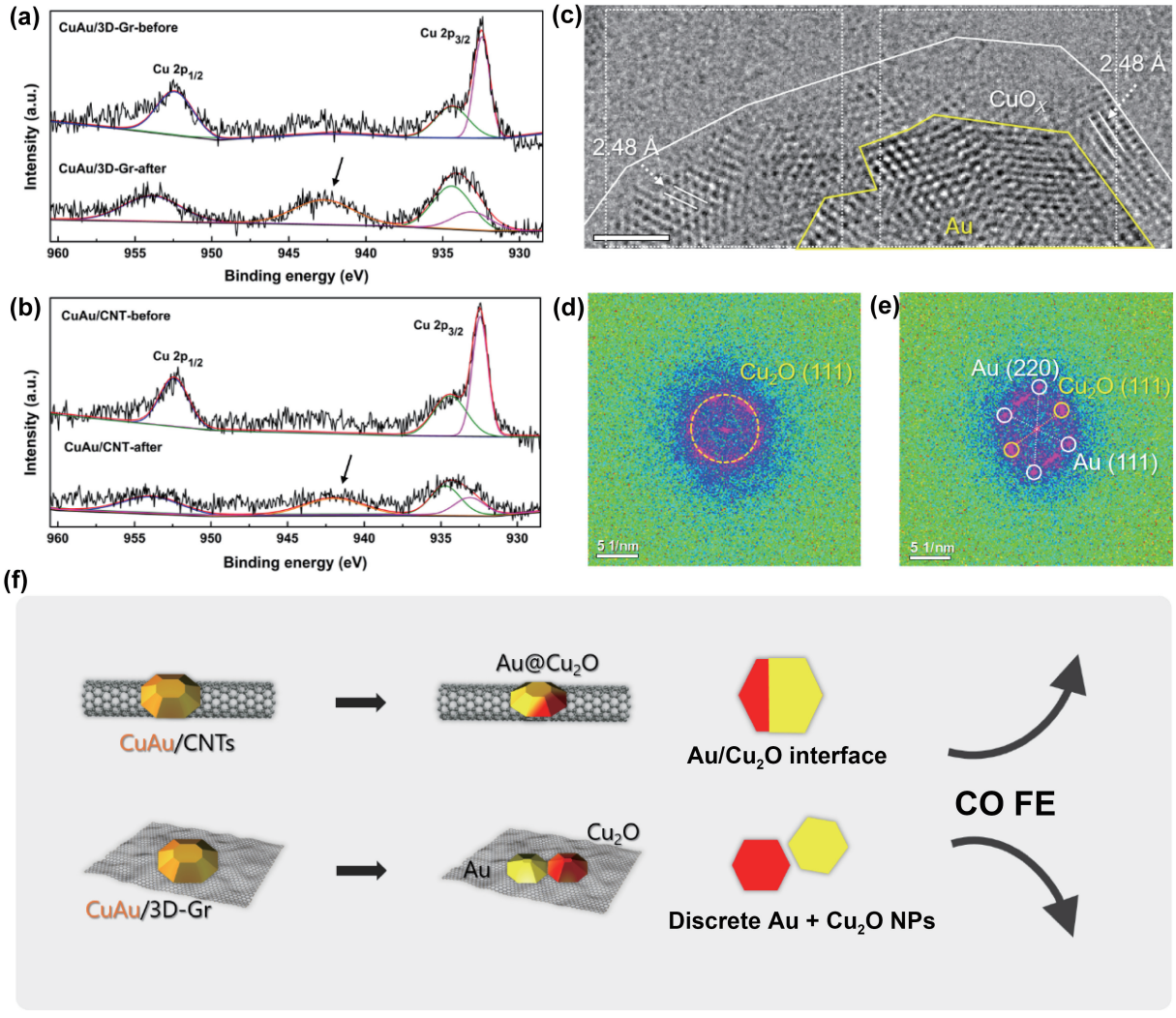

Figure 5 Surface analysis of CuAu nanoparticles. XPS spectra of CuAu/Gr (a) and CuAu/CNT (b). (c) HRTEM image of CuAu/CNT after annealing. (d) and (e) The corresponding FFT pattern on the dashed box on the left side (d) and on the right side (e) in (c). (f) The schematic of phase separation of CuAu NPs in different types of the carbon support leading to different CO FE. The scale bar in (c) is 1 nm.

chemical analyses, we reveal the intimate contact between the segregated CuO_x and CuAu nanoparticles during a moderate phase separation can boost the CO production, while complete spatial separation of CuO_x and Au leads to a poorer CO production. These results provide insights into the fine-tuning of the phase of multi-element nanostructures for electrochemical reduction of CO_2.

Acknowledgements

The authors appreciate the support from the National Natural Science Foundation of China (No. 22172110). We thank the Haihe Laboratory of Sustainable Chemical Transformations for financial support. We thank the facility Center at the Institute of Molecular Plus at Tianjin University to use the transmission electron microscopes.

Electronic Supplementary Material: Supplementary material (detailed experimental methods, TEM and corresponding FFT images, HAADF and EDS mapping images, AES spectra, and stability test) is available in the online version of this article at https://doi.org/10.1007/s12274-022-4935-9.

References

[1] Wei, Z. H.; Sun, J. M.; Li, Y.; Datye, A. K.; Wang, Y. Bimetallic catalysts for hydrogen generation. *Chem. Soc. Rev.* **2012**, *41*, 7994–8008.

[2] Fang, H.; Yang, J. H.; Wen, M.; Wu, Q. S. Nanoalloy materials for chemical catalysis. *Adv. Mater.* **2018**, *30*, 1705698.

[3] Sankar, M.; Dimitratos, N.; Miedziak, P. J.; Wells, P. P.; Kiely, C. J.; Hutchings, G. J. Designing bimetallic catalysts for a green and sustainable future. *Chem. Soc. Rev.* **2012**, *41*, 8099–8139.

[4] Tao, F. Synthesis, catalysis, surface chemistry and structure of bimetallic nanocatalysts. *Chem. Soc. Rev.* **2012**, *41*, 7977–7979.

[5] Zhang, X. B.; Han, S. B.; Zhu, B. E.; Zhang, G. H.; Li, X. Y.; Gao, Y.; Wu, Z. X.; Yang, B.; Liu, Y. F.; Baaziz, W. et al. Reversible loss of core–shell structure for Ni-Au bimetallic nanoparticles during CO_2 hydrogenation. *Nat. Catal.* **2020**, *3*, 411–417.

[6] van der Hoeven, J. E. S.; Jelic, J.; Olthof, L. A.; Totarella, G.; van Dijk-Moes, R. J. A.; Krafft, J. M.; Louis, C.; Studt, F.; van Blaaderen, A.; de Jongh, P. E. Unlocking synergy in bimetallic catalysts by core–shell design. *Nat. Mater.* **2021**, *20*, 1216–1220.

[7] Watanabe, M.; Shibata, M.; Kato, A.; Azuma, M.; Sakata, T. Design of alloy electrocatalysts for CO_2 reduction: III. The selective and reversible reduction of CO_2 on Cu alloy electrodes. *J. Electrochem. Soc.* **1991**, *138*, 3382–3389.

[8] Watanabe, M.; Shibata, M.; Katoh, A.; Sakata, T.; Azuma, M. Design of alloy electrocatalysts for CO_2 reduction: Improved energy efficiency, selectivity, and reaction rate for the CO_2 electroreduction on Cu alloy electrodes. *J. Electroanal. Chem. Interfacial Electrochem.* **1991**, *305*, 319–328.

[9] Friebel, D.; Mbuga, F.; Rajasekaran, S.; Miller, D. J.; Ogasawara, H.; Alonso-Mori, R.; Sokaras, D.; Nordlund, D.; Weng, T. C.;

Nilsson, A. Structure, redox chemistry, and interfacial alloy formation in monolayer and multilayer Cu/Au(111) model catalysts for CO_2 electroreduction. *J. Phys. Chem. C* **2014**, *118*, 7954–7961.

[10] Chen, C. B.; Li, Y. F.; Yu, S.; Louisia, S.; Jin, J. B.; Li, M. F.; Ross, M. B.; Yang, P. D. Cu-Ag tandem catalysts for high-rate CO_2 electrolysis toward multicarbons. *Joule* **2020**, *4*, 1688–1699.

[11] Lv, X. M.; Shang, L. M.; Zhou, S.; Li, S.; Wang, Y. H.; Wang, Z. Q.; Sham, T. K.; Peng, C.; Zheng, G. F. Electron-deficient Cu sites on Cu_3Ag_1 catalyst promoting CO_2 electroreduction to alcohols. *Adv. Energy Mater.* **2020**, *10*, 2001987.

[12] Pardo Pérez, L. C.; Arndt, A.; Stojkovikj, S.; Ahmet, I. Y.; Arens, J. T.; Dattila, F.; Wendt, R.; Guilherme Buzanich, A.; Radtke, M.; Davies, V. et al. Determining structure-activity relationships in oxide derived Cu-Sn catalysts during CO_2 electroreduction using X-ray spectroscopy. *Adv. Energy Mater.* **2022**, *12*, 2103328.

[13] Hoang, T. T. H.; Verma, S.; Ma, S. C.; Fister, T. T.; Timoshenko, J.; Frenkel, A. I.; Kenis, P. J. A.; Gewirth, A. A. Nanoporous copper-silver alloys by additive-controlled electrodeposition for the selective electroreduction of CO_2 to ethylene and ethanol. *J. Am. Chem. Soc.* **2018**, *140*, 5791–5797.

[14] Kim, D.; Resasco, J.; Yu, Y.; Asiri, A. M.; Yang, P. D. Synergistic geometric and electronic effects for electrochemical reduction of carbon dioxide using gold-copper bimetallic nanoparticles. *Nat. Commun.* **2014**, *5*, 4948.

[15] He, J. F.; Johnson, N. J. J.; Huang, A. X.; Berlinguette, C. P. Electrocatalytic alloys for CO_2 reduction. *ChemSusChem* **2018**, *11*, 48–57.

[16] Lee, S.; Park, G.; Lee, J. Importance of Ag-Cu biphasic boundaries for selective electrochemical reduction of CO_2 to ethanol. *ACS Catal.* **2017**, *7*, 8594–8604.

[17] Wang, Y.; Wang, D. G.; Dares, C. J.; Marquard, S. L.; Sheridan, M. V.; Meyer, T. J. CO_2 reduction to acetate in mixtures of ultrasmall $(Cu)_n(Ag)_m$ bimetallic nanoparticles. *Proc. Natl. Acad. Sci. USA* **2018**, *115*, 278–283.

[18] Huang, J. F.; Mensi, M.; Oveisi, E.; Mantella, V.; Buonsanti, R. Structural sensitivities in bimetallic catalysts for electrochemical CO_2 reduction revealed by Ag-Cu nanodimers. *J. Am. Chem. Soc.* **2019**, *141*, 2490–2499.

[19] Tao, Z. X.; Wu, Z. S.; Yuan, X. L.; Wu, Y. S.; Wang, H. L. Copper-gold interactions enhancing formate production from electrochemical CO_2 reduction. *ACS Catal.* **2019**, *9*, 10894–10898.

[20] Wang, L.; Higgins, D. C.; Ji, Y. F.; Morales-Guio, C. G.; Chan, K.; Hahn, C.; Jaramillo, T. F. Selective reduction of CO to acetaldehyde with CuAg electrocatalysts. *Proc. Natl. Sci. USA* **2020**, *117*, 12572–12575.

[21] Ren, D.; Ang, B. S. H.; Yeo, B. S. Tuning the selectivity of carbon dioxide electroreduction toward ethanol on oxide-derived Cu_xZn catalysts. *ACS Catal.* **2016**, *6*, 8239–8247.

[22] Kim, D.; Xie, C. L.; Becknell, N.; Yu, Y.; Karamad, M.; Chan, K.; Crumlin, E. J.; Nørskov, J. K.; Yang, P. D. Electrochemical activation of CO_2 through atomic ordering transformations of AuCu nanoparticles. *J. Amer. Chem. Soc.* **2017**, *139*, 8329–8336.

[23] Chang, C. J.; Hung, S. F.; Hsu, C. S.; Chen, H. C.; Lin, S. C.; Liao, Y. F.; Chen, H. M. Quantitatively unraveling the redox shuttle of spontaneous oxidation/electroreduction of CuO_x on silver nanowires using *in situ* X-ray absorption spectroscopy. *ACS Cent. Sci.* **2019**, *5*, 1998–2009.

[24] Zhang, L. J.; Li, M.; Zhang, S. B.; Cao, X. R.; Bo, J. X.; Zhu, X. L.; Han, J. Y.; Ge, Q. F.; Wang, H. Promoting carbon dioxide electroreduction toward ethanol through loading Au nanoparticles on hollow Cu_2O nanospheres. *Catal. Today* **2021**, *365*, 348–356.

[25] Lee, C. W.; Yang, K. D.; Nam, D. H.; Jang, J. H.; Cho, N. H.; Im, S. W.; Nam, K. T. Defining a materials database for the design of copper binary alloy catalysts for electrochemical CO_2 conversion. *Adv. Mater.* **2018**, *30*, 1704717.

[26] Jeon, H. S.; Timoshenko, J.; Scholten, F.; Sinev, I.; Herzog, A.; Haase, F. T.; Roldan Cuenya, B. Operando insight into the correlation between the structure and composition of CuZn nanoparticles and their selectivity for the electrochemical CO_2 reduction. *J. Am. Chem. Soc.* **2019**, *141*, 19879–19887.

[27] Chang, C. J.; Lin, S. C.; Chen, H. C.; Wang, J. L.; Zheng, K. J.; Zhu, Y. P.; Chen, H. M. Dynamic reoxidation/reduction-driven atomic interdiffusion for highly selective CO_2 reduction toward methane. *J. Am. Chem. Soc.* **2020**, *142*, 12119–12132.

[28] Ye, K.; Zhou, Z. W.; Shao, J. Q.; Lin, L.; Gao, D. F.; Ta, N.; Si, R.; Wang, G. X.; Bao, X. H. *In situ* reconstruction of a hierarchical Sn-Cu/SnO_x core/shell catalyst for high-performance CO_2 electroreduction. *Angew. Chem., Int. Ed.* **2020**, *59*, 4814–4821.

[29] Zhan, W. C.; Wang, J. L.; Wang, H. F.; Zhang, J. S.; Liu, X. F.; Zhang, P. F.; Chi, M. F.; Guo, Y. L.; Guo, Y.; Lu, G. Z. et al. Crystal structural effect of AuCu alloy nanoparticles on catalytic CO oxidation. *J. Am. Chem. Soc.* **2017**, *139*, 8846–8854.